Research Article

Evolution mechanisms of microstructure and mechanical properties in a friction stir welded ultrahigh-strength quenching and partitioning steel

Z.W. Wang [a,b], J.F. Zhang [a], G.M. Xie [c], L.H. Wu [a], H. Zhang [a], P. Xue [a,*], D.R. Ni [a], B.L. Xiao [a], Z.Y. Ma [a]

[a] *Shi-changxu Innovation Center for Advanced Materials, Institute of Metal Research, Chinese Academy of Sciences, Shenyang 110016, China*
[b] *School of Materials Science and Engineering, University of Science and Technology of China, Shenyang 110016, China*
[c] *State Key Laboratory of Rolling and Automation, Northeastern University, Shenyang, 110819, China*

A B S T R A C T

Ultrahigh-strength quenching and partitioning (Q&P) steels have attracted strong interests in the auto manufactory, while the comprehensive understanding in the microstructure and mechanical behavior of their welded joints is highly needed to enrich their applications. In the present work, it is designed to make an insight into these imperative conundrums. Equal strength Q&P 1180 steel joints to parent metal were successfully fabricated via friction stir welding (FSW) technique under different parameters. Apparent hardening and softening were observed in stir zone (SZ) and heat-affected zone (HAZ) respectively, whose microstructures strongly depended on the peak temperature and cooling rate during welding. The formation of fresh martensite was the main mechanism for the SZ hardening, while the decomposition of metastable phases played key roles in the microhardness drop of the HAZ. A heat source zone-isothermal phase transition layer model was proposed to clarify the impregnability of the joint strength under parameter variation. The dual-phase structure, nano-carbide particles, tempered initial martensite, and ultrafine-grained ferrite synergistically improved the strain hardening ability of the HAZ, which eventually resulted in the equal strength FSW joints.

© 2021 Published by Elsevier Ltd on behalf of Chinese Society for Metals.

1. Introduction

Quenching and partitioning (Q&P) is a new heat treatment process which was proposed by Speer et al. [1] to improve the mechanical properties of steels. It is based on a new recognition that carbon can penetrate from martensite/bainite into austenite below the martensite start temperature (M_s) [2]. This process can produce carbon-rich retained austenite (RA) for utilizing the transformation-induced plasticity (TRIP) effect and enhancing the strength-ductility trade-off of steels [3]. Q&P steel, one kind of the third generation automotive steels, produced via the Q&P process, is promising to promote weight reduction, energy savings, and passive safety improvement. Currently, commercial Q&P 1180 steel with ultrahigh-strength (over 1000 MPa) has been mass-produced by Baosteel Co., Ltd. in China.

Up to now, most of the reported works have concentrated on the microstructure and mechanical properties of the Q&P steels.

Tan et al. [4] analyzed the microstructure-properties relationship in ultrahigh-strength Q&P steel and found that the retained austenite could decrease the elastic limit and yield strength. Furthermore, both the dislocations interaction and the TRIP effect improved the work hardening rate, ultimate strength (UTS) and uniform elongation (UE). Diego-Calderón et al. [5] studied the effect of microstructural architecture on the fracture behavior of multiphase Q&P steels. They addressed that the fracture properties of Q&P steels could be designed via manipulating the volume fraction and morphology of retained austenite and matrix conditions.

However, few works have focused on the evolution of microstructures and mechanical properties of the Q&P steels during subsequent processing, such as welding, which is a crucial manufacturing procedure in assembling parts. Currently, there are prominent challenges in the welding process of advanced ultrahigh-strength steels (AUHSSs) because the non-equilibrium phases like martensite, bainite or retained austenite are the characteristic microstructures in these high-performance steels [6–8]. These metastable phases can worsen the weldability of steels due to their temper softening effect during welding thermal cycle. During fusion welding using conventional methods like gas metal arc

---

* Corresponding author.
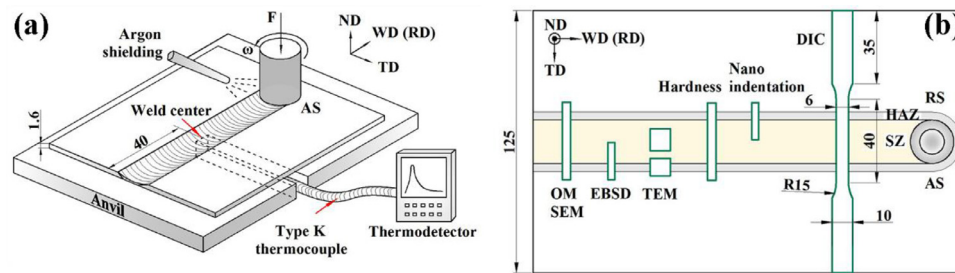 *E-mail address:* pxue@imr.ac.cn (P. Xue).

Fig. 1. Schematics of (a) welding configuration and thermal measurement, (b) sampling methods for characterizing the microstructure and mechanical properties. ND and TD are the abbreviations of the normal direction and the transverse direction, respectively.

welding (GMAW) and laser welding (LW), the original microstructures of 1500 MPa and 1700 MPa grades of AUHSSs were totally destroyed and the significant loss of the superior properties of the parent metal (PM) could be easily detected among the joints [9,10].

Improving the weldability of the third generation automotive steels, which is mainly instantiated in the enhancement of the joint strength, is crucial to enable the wide application of this group of advanced steels. Nevertheless, there are limited reports on the welding of Q&P steels to our best knowledge. Recently, Guo et al. [11,12] revealed that the strength of fiber laser welded Q&P 980 steel joints were not degraded for the less softening in the heat-affected zone (HAZ). They found that the HAZ contained partially tempered martensite with hardness drops of less than 37 Hv. All the joints failed at the PM with near 100% joint efficiency (JE, the UTS ratio of the joint to the PM). However, the weldability of the ultrahigh-strength Q&P steels, for instance the Q&P 1180 steel, is still not clear. Compared to Q&P 980 steel, these steels exhibit higher fraction of the metastable phases together with finer grains, making their weldability more challenging.

Apart from the intrinsic material attribute, the welding method also has a vital influence on the joint quality of the AUHSSs. As a solid-state joining technique with low heat input, friction stir welding (FSW) can avoid the fusion-solidification induced defects during the GMAW or LW, and thus improve the joint properties of the AUHSSs [13,14]. Besides, the FSW procedure involves the effect of grain refinement, which can obviously suppress the grain growth of the welded joint [15,16]. Furthermore, the peak temperature can be flexibly controlled via FSW parameters so as to adjust the phase composition of the joint, signifying the feasibility of sustaining the as-received microstructures of the AUHSSs [17,18]. Therefore, the FSW technology was employed in this study for fabricating high-quality Q&P 1180 steel joints, while the evolution of microstructures and mechanical properties as well as associated weldability of the Q&P 1180 steel were systematically investigated.

The objectives of this study are to (a) verify whether high-quality Q&P steel joints could be achieved via the FSW technology, (b) examine the microstructures, mechanical properties and underlying mechanisms during the FSW process, and (c) establish the relationship and interactive regularity among the welding heat input, microstructures and mechanical properties.

2. Experimental procedures

2.1. Welding configuration

The cold-rolled Q&P 1180 steel sheets with a thickness of 1.6 mm chemical composition listed in Table 1 were used as the PM. FSW, as schematically illustrated in Fig. 1(a), was implemented using a displacement-controlled machine with a spindle tilt angle of 1.5°. A W-25Re alloy stir tool with 11 mm in shoulder diameter and 5 mm in pin root diameter was used. We designed the welding parameters considering the welding window commonly used during

Table 1
Chemical composition (wt%) of the Q&P 1180 steel.

C	Mn	Si	Al	S	P	Fe
0.19	2.76	1.60	0.039	0.003	0.01	Bal.

FSW of steels (300–800 rpm for rotation rates, 25–400 mm/min for moving speeds [13,16,17,19,20]). So the tool rotation rates of 450 rpm and 600 rpm were adopted to adjust welding heat input. In order to ensure defect-free joints, an intermediate moving speed of 200 mm/min was selected. The moving direction of the tool, i.e. the welding direction (WD), was parallel to the rolling direction (RD) of the PM. Argon was used as the shielding gas to prevent the joints from being oxidized during welding.

2.2. Microstructure and hardness

As shown in Fig. 1(b), the microstructural observations were performed on the cross-sections of joints (TD × ND plane) by optical microscopy (OM, Leica DMi8M), scanning electron microscopy (SEM, Zeiss Supra 55) which equipped with an electron backscatter diffraction (EBSD, Channel 5 software) module, and transmission electron microscope (TEM, FEI Tecnai F20). EBSD data was acquired at a step size of 0.2 μm and grain size was measured via a linear intercept method. Misorientation angles between 2–15° were adopted to define the low angle grain boundaries (LAGBs). The specimens for OM and SEM observation were mechanically ground, polished and etched with 5% Nital. The samples for EBSD experiments were mechanically polished in silica soliquoid followed by electro-polishing in 10% perchloric acid + 90% ethanol solution. All of the SEM and EBSD observations were operated at the thickness center on the advancing side (AS). TEM films were prepared by twin-jet thinning using the same solution as EBSD preparation at -25°C under a potential of 20 V. Electron probe microanalysis (EPMA, JEOL 5853) was conducted to represent the element distributions, and X-ray diffraction (XRD, Cu radiation, 4 °/min in counting rate) was utilized to quantify the retained austenite using the five peaks method [21]. Vickers microhardness was measured on the polished specimens along with the thickness center under an applied load of 200 g with a dwell time of 15 s.

2.3. Temperature history

In order to examine the temperature history of the whole FSW joint, a heat transfer simulation near the joint was carried out via finite element method. The generation rate q of the friction heat between the workpiece and the tool was defined as

$$q = \mu(T)p\frac{2\pi\omega}{60}r \tag{1}$$

where μ is the friction coefficient, T is the temperature, p is the pressure between workpiece and the tool, ω is the revolutions per

minute, r is the radius of the heating region. The corresponding governing equation and the boundary conditions were built and set referring to the models proposed by Zhang et al. [22] and Wu et al. [23].

To adjust the simulation parameters, the temperature history were also measured using thermocouple. A type K thermocouple was placed on the back of the weld center to measure the thermal cycles of the stir zone (SZ). Before welding, an anvil which was slotted perpendicular to the welding direction was prepared to guide the thermocouple (Fig. 1(a)). At the end of the slot, a minor groove was machined and the thermocouple tip was then placed in the groove and aligned with the weld center. A frequency of 100 Hz was adopted to collect the temperature data during welding. One thing should be noted here is, the measured results were generally lower than the simulated values (compare Figs. S1 with 8), because of the temperature difference existed between the surface and interior of weld and the heat loss via the slotted anvil. Hence, it would be better to use the simulation results to analyze the temperature history of the whole joint.

2.4. Tensile and DIC test

Digital image correlation (DIC) technique enables a quantitative investigation of partial strain partitioning on a material surface during tensile deformation [24,25]. In this work, two high-speed cameras with Schneider 50 mm f/3D lens were used to capture the upper surface of the joint, and the acquisition frequency was consistent with five images per second. Reger RGM-2010 tensile machine was used to produce uniaxial tensile strain at an initial strain rate of 1×10^{-3} s^{-1}. The sample morphology for the DIC test is shown in Fig. 1(b). It should be pointed out that the strength and elongation of the joints were extra assessed in Instron 8801 testing system with the same strain rate and sample morphology as the DIC test. At least three samples were tested for each welding parameter to verify the accuracy of the results.

2.5. Nanoindentation

Agilent G200 nanoindenter, which was equipped with a Berkovich indenter with 20 nm curvature radius, was used to obtain the displacement-load response of particular phases. 10×10 indentation matrixes with a distance of 2 μm between adjacent points were performed on the electro-polished sample surface. The load-displacement curves were recorded under a consistent peak load of 1.5 mN, a surface approach velocity of 10 nm/s and a peak hold time of 10 s. After the indentation test, the sample surface was first slightly etched with 5% Nital, and then the SEM was used for matching the regardful phases and the indents.

3. Results

After FSW, defect-free joints with full penetration were successfully fabricated under both of the 450 rpm and 600 rpm parameters. As shown in the cross-sectional macrostructures of Fig. 2(a–d), three typical zones, i.e. the SZ, HAZ and PM were identified. The inhomogeneous HAZ could be subdivided into three zones as the distance away from the SZ, namely fine-grained HAZ (FG-HAZ, only visible for the 600 rpm joint), inter-critical HAZ (IC-HAZ) and sub-critical HAZ (SC-HAZ). Fig. 3 and Table 2 exhibit the microhardness distribution and the typical hardness values of the two FSW joints, respectively. It was clear that, compared with the PM, the SZs showed obvious hardening with higher hardness values, while the HAZs showed conspicuous softening with lower hardness values. A detailed description of the sub-HAZ widths via background colors in Fig. 3 indicated that a broader HAZ was obtained in the 600 rpm joint than that of the 450 rpm joint, and there
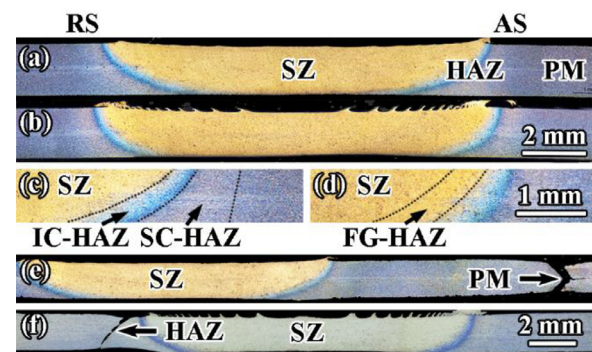

Fig. 2. Cross-sectional images of FSW joints under 450 rpm (a,c,e) and 600 rpm (b,d,f) parameters.
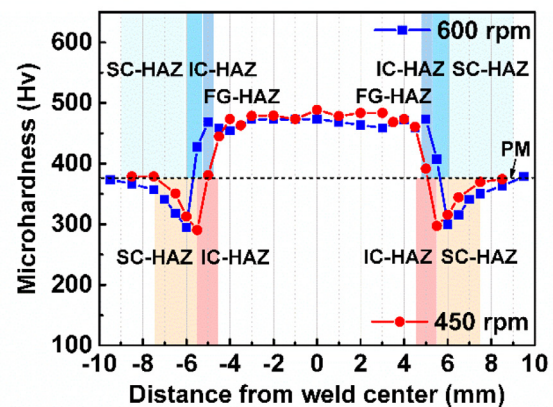

Fig. 3. Cross-sectional microhardness distribution of FSW joints.

was a gradual increase of width varying from the FG-HAZ to the SC-HAZ. Besides, the tensile properties in Table 2 which were extracted in Fig. S2 revealed that the FSW joints showed comparable UTS to the PM, while final failure occurred at the PM or the HAZ (Fig. 2(e,f)). In other words, full-strength joints were achieved although the HAZs suffered obvious softening. To understand underlying mechanisms behind this excellent behavior, the microstructural features of the PM, SZ and HAZ were characterized in detail.

3.1. Parent material

The microstructural features in Fig. 4 indicated that the PM consisted of irregular ferrite (F) and lath martensite. Most of the ferrite grains were several micrometers in size. It is specially noted that there were two kinds of martensite phases in the PM. The initial martensite (M_I) showed lamellar morphology and formed during the quenching process before partitioning, while the fresh martensite (M_F) formed during the final quenching process after partitioning. Based on different etching behavior, the easily etched martensitic matrix was the M_I and the blocky phase with a smooth morphology was the M_F [26], as shown in Fig. 4(a). In the kernel average misorientation (KAM) map of Fig. 4(b), the martensite showed higher KAM than the ferrite, which can be attributed to higher density of geometrically necessary dislocations (GNDs) stored in martensite [27].

Retained austenite with polygonally ultrafine structure (Fig. 4(b), colored in red) was found at the prior austenite grain boundaries (PAGBs) and its volume fraction was ~8.6% based on the XRD analysis (Fig. 4(c)). Except for the polygonal morphology, smaller retained austenite with lamellar structure which was hard to be detected by the EBSD was observed between the M_I laths in

Table 2
Mechanical properties of the PM and the FSW joints.

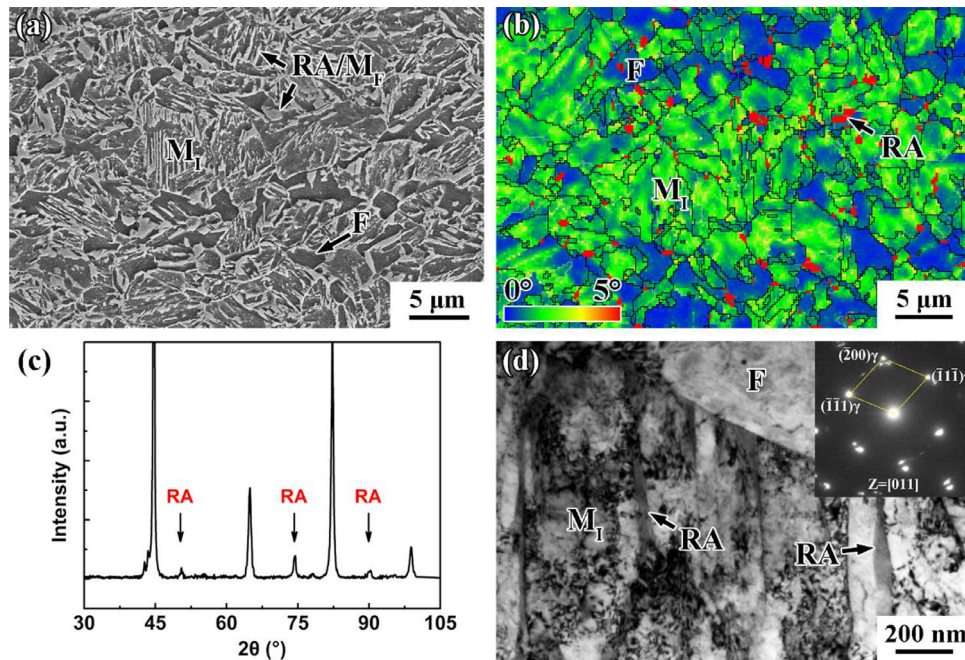| Materials	Average hardness in SZ (Hv)	Minimum hardness in HAZ (Hv)	UTS (MPa)	Failure location
PM	376	-	1214±5	PM
450 rpm joint	477	290	1212±4	PM
600 rpm joint	466	295	1208±8	HAZ

Fig. 4. (a) SEM image, (b) EBSD KAM combined with phase map, (c) XRD pattern and (d) TEM image of the PM.

TEM image (Fig. 4(d)). In addition, although the partitioning heat treatment had been operated, carbide (C) particles were hard to found in the PM due to the addition of Si that inhibited the carbide formation [28]. According to the numerical model proposed by Trzaska and Dobrzański [29], the A_{c1} and A_{c3} phase transformation temperatures of the PM were calculated as 746 °C and 847 °C, respectively. The predicted minimum cooling rate between 800 °C and 500 °C that is necessary for fully martensitic transformation was 12.9 °C/s [19]. This critical cooling rate together with the two phase transformation temperatures played crucial roles in determining the phase composition across the welds.

3.2. Stir zone

In the SZ, single-phase M_F with lath substructure formed without precipitated carbide particles, while the ferrite and retained austenite was not found (Fig. 5). The M_F in the 600 rpm joint was coarser than that in the 450 rpm joint via singularizing the PAGBs with white dotted lines (Fig. 5(a, d)). In the EBSD inverse pole figures (IPFs) of Fig. 5(b, e), no obvious preferred orientation was observed for the M_F in both of the SZs. High density of LAGBs were produced in the whole M_F, as displayed with white solid lines. The TEM morphology confirmed the formation of the lath martensite with profuse dislocations, and the lath width of the 600 rpm joint was larger than that of the 450 rpm joint (Fig. 5(e, f)).

3.3. Heat affected zone

In the HAZ, similar microstructural features were observed in the 450 rpm and 600 rpm joints for the IC-HAZ and SC-HAZ. The IC-HAZ of 450 rpm joint showed a DP structure of ferrite and

martensite. Similar to the M_F in the PM, the martensite in this region was also in a quenched state and showed smooth morphology (Fig. 6(a)) with high KAM (Fig. 6(d)) and dislocation density (Fig. 6(g)). By means of the point counting method [30], the ferrite proportion in the HAZ was measured from the SEM images at different locations. The results in Fig. 7 display a gradual increase of the ferrite proportion with the distance away from the weld center. The volume fraction of ferrites reached a maximum at the boundary of the IC-HAZ and the SC-HAZ.

For the SC-HAZ, no palpable distinction on the micromorphology was detected in the SEM image of Fig. 6(b), compared to the PM. Whereas, the inset in Fig. 6(b) shows that plenty of carbide particles precipitated along the PAGBs, and the M_F could still be found. As shown in Fig. 7, the volume fraction of ferrites measured in this region exhibited an incremental trend towards the weld center. The EBSD KAM combined with the phase map of Fig. 6(e) indicated that almost all of the retained austenite in the PM was dissolved after welding (similar result was obtained during the XRD testing), and the lamellar retained austenite that commonly existed in the PM was rarely observed in the TEM image (Fig. 6(h)). In the inset of Fig. 6(h), the precipitated particles were M_3C type carbide and presented short rod-like shapes with nanoscale sizes, as reported in our previous work [31].

Different from the above two sub-HAZs, full M_F structure that was analogous to that in the SZs formed in the FG-HAZ of 600 rpm joint (Fig. 6(c)). As profiled with white dotted lines in Figs. 5(d) and 6(c), the martensite sizes in the FG-HAZ were smaller than those in the SZ of 600 rpm joint but were similar to those in the SZ of the 450 rpm joint (Fig. 5(a)). In Fig. 6(f), the FG-HAZ exhibited high KAM value, which was higher than both the IC-HAZ and the SC-HAZ due to the existence of more M_F phase.
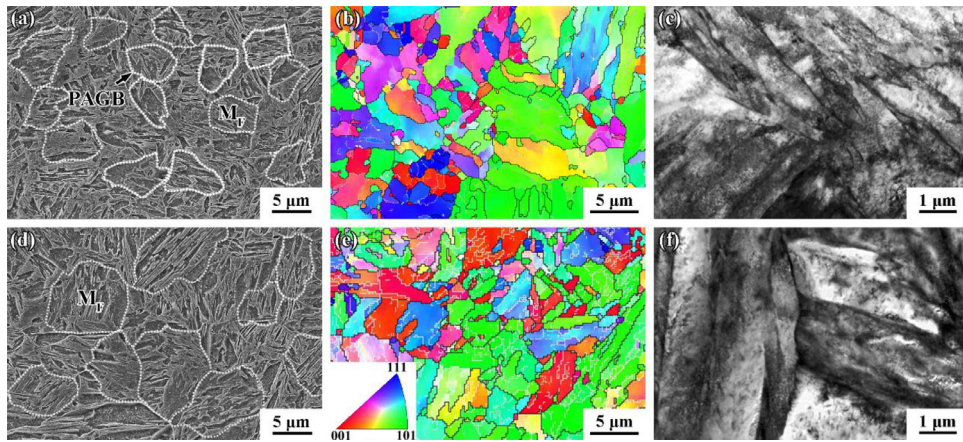
Fig. 5. (a) SEM, (b) EBSD IPF map and (c) TEM microstructures of the SZ under 450 rpm parameter, (d) SEM, (e) EBSD IPF map and (f) TEM microstructures of the SZ under 600 rpm parameter.
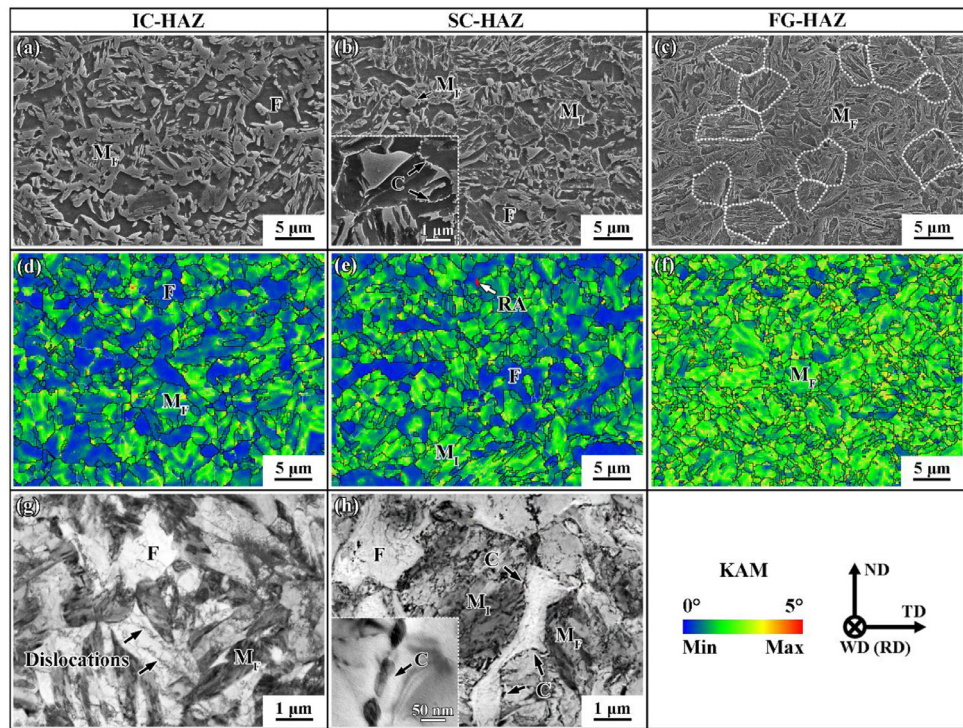

Fig. 6. Microstructures of the three sub-HAZs: (a)–(c) SEM surface topography images, (d)–(f) typical EBSD KAM together with phase maps, (g, h) TEM maps.

3.4. Temperature fields

Fig. 8(a, b) presented the simulated temperature fields of the whole FSW joints. Based on the cross-sectional temperature distributions in Fig. 8(b), compared to the 450 rpm joint, the 600 rpm joint exhibited wider SZ and SC-HAZ due to higher heat input. However, there were no obvious difference in the IC-HAZ width (between A_{c3}-A_{c1} region), which was consistent with the cross-sectional macrostructure shown in Fig. 2. The temperature curves of different zones were extracted from the simulated results (points A-D in Fig. 8(b)) to present the local thermal cycles, as exhibited in Fig. 8(c, d).

As for the temperature curves of the SZs during welding, it was distinct that the SZs undertook rapid heating, short isothermal insulation and cooling cycles. After the rapid heating, the peak temperatures of both the 450 rpm and 600 rpm joints were higher than the A_{c3} temperature. Based on the temperature curves, the

Table 3
Calculated cooling rates of different zones in the simulated results (°C/s).

Sample	SZ	FG-HAZ	IC-HAZ	SC-HAZ
450 rpm joint	272.7	-	162.8	143.2
600 rpm joint	263.1	142.2	141.3	110.5

cooling rates (800–500 °C) were calculated with the results of 272.7 °C/s and 263.1 °C/s for the 450 rpm and 600 rpm joints, respectively (Table 3), both of which were significantly higher than the minimum cooling rate for the fully martensitic transformation (12.9 °C/s). Similar high cooling rates for the martensitic transformation were attained in HAZs, including the FG-HAZ (peak temperature over the A_{c3}), IC-HAZ (peak temperature between the A_{c1} and A_{c3}), and the SC-HAZ (peak temperature below the A_{c1}).
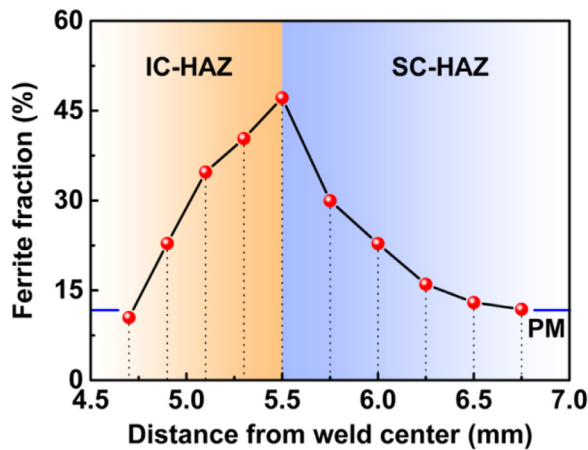
Fig. 7. Ferrite fraction distributions in the HAZ for the 450 rpm joint.

3.5. DIC and nanoindentation

The extensional strain distributions measured in the upper joint surfaces as a function of accumulated tensile strain were summarized in Fig. 9(a, b). On behalf of quantifying the local strains, the local axial strain profiles were extracted and drawn in Fig. 9(c, d). The stress concentrations in Fig. 9 were unrelated to the AS or retreating side (RS) of the joints because random fractures at the both sides were found during the tensile tests. The results displayed that during the elastic loading stage (0.4% tensile strain), the HAZs possessed striking strain concentrations (arrows in Fig. 9(a,b)), indicating nearly all 0.4% strain was only applied in the soft HAZ. Near the yielding stage (0.76% tensile strain), the plastic strains sequentially encompassed the HAZs. In the subsequent work hardening stage (5% tensile strain), however, the PM regions also underwent plastic strain that was comparable to that in the HAZs. This phenomenon was recommended to be involved in the strain hardening effect which resulted in a gradual increase

Table 4
Detailed nanoindentation results and the consequent parameters obtained during the inverse calculation.

	Phase	E (GPa)	H (GPa)	σ_y (MPa)	n
PM	F	198	2.82	292	0.17
	M_I	244	5.27	763	0.04
	M_F	307	7.26	1147	-0.03
SC-HAZ	F	213	3.31	386	0.12
	M_I	225	5.09	729	0.07
	M_F	301	7.10	1115	-0.01

of effective stress in the HAZ to a final equilibrium with the PM region [32,33]. After this stage, necking gradually occurred and the plastic strain was mostly sustained by the PM region for the 450 rpm joint and by the HAZ for the 600 rpm joint, respectively. Noteworthily, both of the SZs experienced almost no plastic strain, and the local strain distributions across the joints were unsymmetrical during the whole tensile procedures. The unsymmetrical local strain distributions were presumably attributable to (a) the unsymmetrical loading mode of current uniaxial testing equipment (uniform elongation stages of 0.4%, 5%) and (b) necking which could produce strain localization at high tensile strain stages (9.3 and 11% for 450 rpm joint, 7.2 and 8% for 600 rpm joint).

Nanoindentation testing was performed on the SC-HAZ and PM to clarify the micro-properties evolution of certain phases. Based on the load-displacement data in Fig. 10(a), stress-strain curves were calculated and exhibited in Fig. 10(b) via the previously well-developed inverse method [34–37]. Table 4 lists the parameters obtained during the inverse calculation. It was evident that the M_I and M_F possessed higher elastic modulus (E) and nanohardness (H) than the ferrite, which might be associated with their higher GND density and lath structures (Fig. 4(b,c)). Compared with the PM, no distinct difference was observed in the elastic modulus, nanohardness and yield strength (σ_y) between the M_I and the M_F, while conspicuous increase of these parameters was detected for the ultrafine ferrite in the SC-HAZ. As revealed in Fig. 10(b), the strain hardening ability (embodied via hardening exponent n in Table 4)
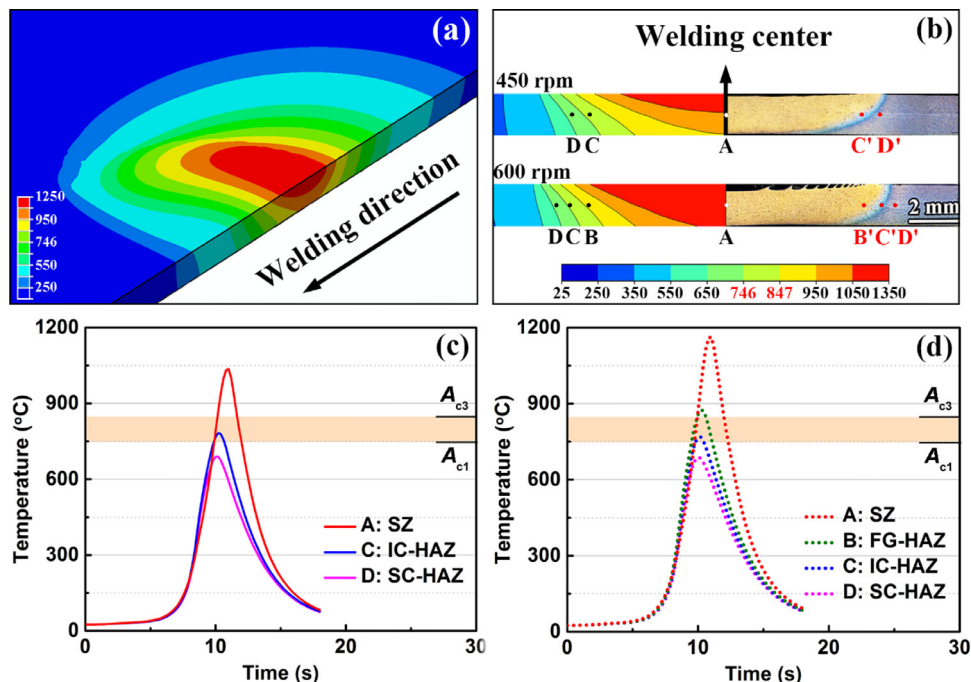

Fig. 8. Temperature variations of the FSW joints simulated by finite element method: (a) 3D temperature distribution, (b) cross-sectional temperature distributions, (c,d) temperature-time curves of different zones measured from the corresponding points in (b).
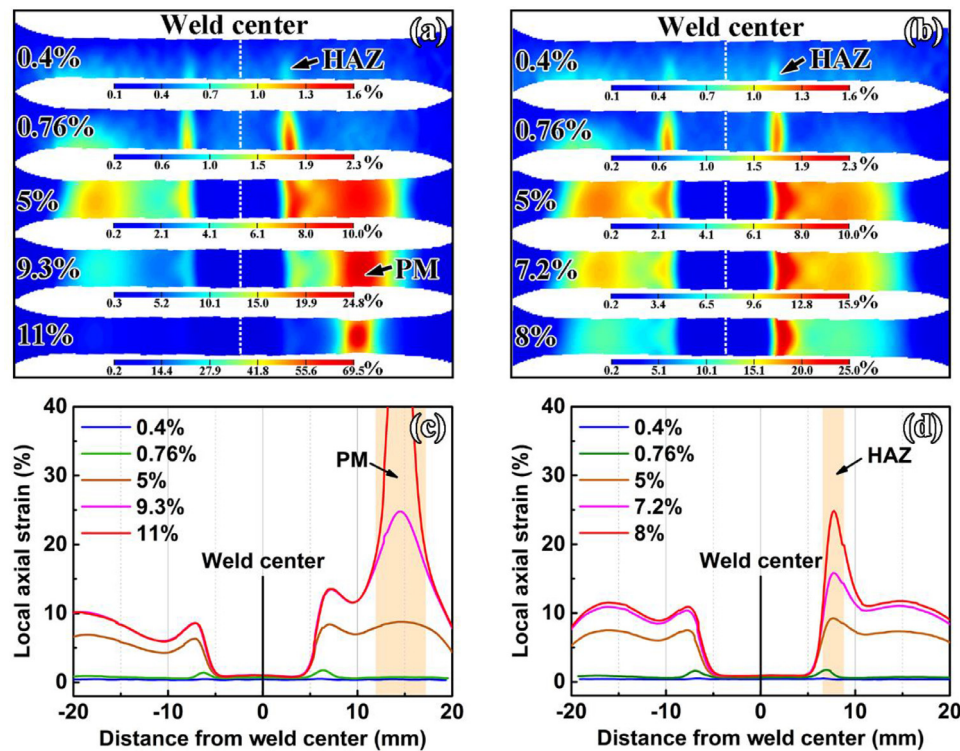
Fig. 9. Upper surface strain distributions of joints during tensile deformation: (a,b) local strain distribution maps, (c,d) local axial strain profiles extracted in the strain distribution maps along with the TD of gauge center. (a,c) and (b,d) act for the 450 rpm and 600 rpm joints, respectively.
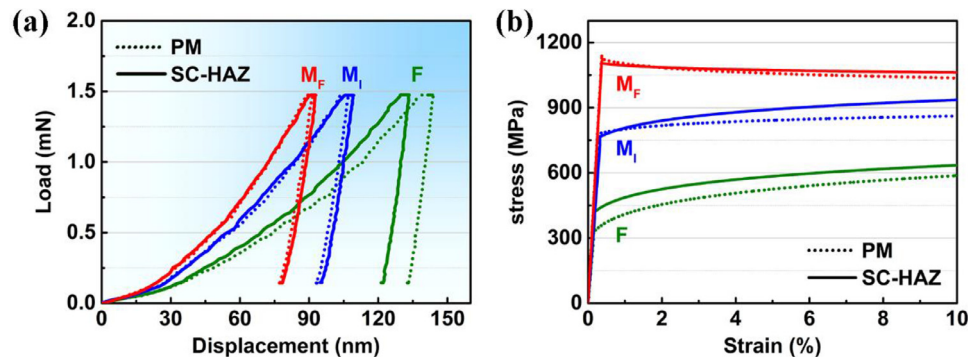

Fig. 10. Nanoindentation results of the SC-HAZ (450 rpm joint) contrasting with the PM: (a) load-displacement curves of typical ferrite and martensite phases, (b) stress-strain curves that were calculated based on the inverse method.

of the martensite, especially the M_I, was improved after the FSW thermal cycling treatment.

4. Discussion

4.1. Macromorphology evolution of the joints

Based on Figs. 2 and 3, it is clear that the SZ and the SC-HAZ expanded as increasing the welding heat input, and the HAZ moved outward relative to the weld center at a higher rotation rate of 600 rpm. However, the softening degree and strength of the joints were not influenced by the rotation rates as shown in Table 2. Similarly, Liu et al. [38] declared that the tensile strength and HAZ hardness values of the welds were independent of the tool rotation rate during FSW of an aluminum alloy, and a heat source zone-isothermal dissolution layer model was proposed to explain it. In current work, a modified model, which was named heat source zone-isothermal phase transition layer (HSZ-IPTL) model, was suggested in the FSW joints of Q&P steels. As

shown in the schematic of Fig. 11, the SZ that located just below the tool shoulder with a basin shape could be regarded as the HSZ. The HAZs, which only experienced thermal exposure without mechanical stirring, were regarded as the IPTLs.

As the FSW proceeding, material softening and hardening could occur around the HSZ due to thermal exposure, resulting in the generation of the different hardness zones. The low hardness zones that experienced approximately the same peak temperature below A_{c3} (Fig. 8(b)) were always produced at various rotation rate due to lower peak temperature than the HSZ. Under this circumstance, the low hardness zones were involved in the IPTLs, which corresponded to the temperature ranges of A_{c3}-A_{c1} (IC-HAZ) and $< A_{c1}$ (SC-HAZ), as shown in Fig. 11(a). The IPTLs possessed similar softening degree due to similar microstructures obtained in comparable peak temperature. Thus, similar joint strength was achieved although the welding rotation rate was altered.

The FG-HAZ was also involved in the IPTLs although the ceiling temperature of the FG-HAZ was hard to determined due to the ambiguous relationship between the microstructure and temperature
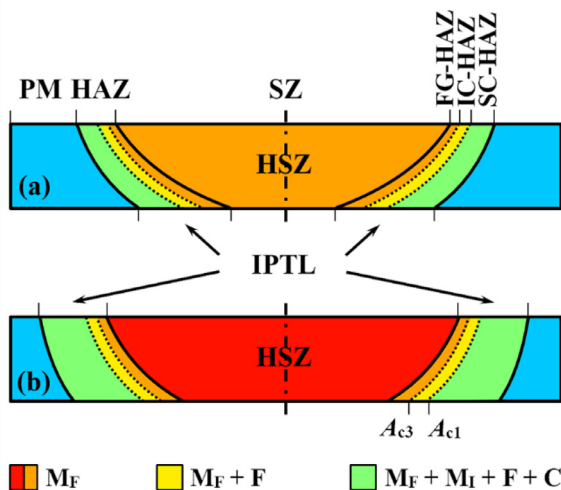
Fig. 11. Schematic of the HSZ-IPTL model: (a) 450 rpm joint, (b) 600 rpm joint.

history. Considering the similar micro morphologies and hardness in the SZ and the FG-HAZ under 450 rpm and 600 rpm joints, respectively (see Figs. 5(a), 6(c) and 3), it was acceptable that the FG-HAZ was actually developed in the 450 rpm joint but was hardly differentiated from the microstructure of the SZ. In this case, the IPTL model was also practicable to elucidate the evolution of the joint's properties. In addition, higher temperature induced further heat diffusion, thence produced larger HSZ and IPTL with broader SZ and SC-HAZ in the 600 rpm joint than that in the 450 rpm joint (Fig. 11(b))

4.2. Material hardening during welding

Fig. 3 displayed distinct hardening behaviors of the SZs and the FG-HAZs which possessed higher hardness than the PM region after the FSW process. Ghosh et al. [39] proposed that the SZ microstructure depended on the peak temperature and cooling rate during welding. In present study, the peak temperature (Fig. 8(c, d)) and cooling rate (Table 3) in the SZs indicated that complete austenitizing and subsequent fully martensitic transformation occurred, causing a microstructural change from multiphase structures of the PM (Fig. 4) to single-phase M_F of the SZs. Thus, significant hardening via martensite phase transformation was achieved in the SZs. In addition, lower heat input (Fig. 8(b–d)) for the 450 rpm joint inhibited the growth of prior-austenite grains under minor peak temperature, causing the finer M_F in the 450 rpm SZ than that in the 600 rpm SZ (Fig. 5).

Compared with the SZ, the FG-HAZ possessed higher microhardness with finer M_F structure due to lower peak temperature (Fig. 3), which could be verified by the EBSD statistical results: average grain size of 0.83 μm for the FG-HAZ and 1.10 μm for the SZ under the 600 rpm parameter. This phenomenon was also associated with the low temperature induced growth-inhibiting effect of the prior-austenite grains. Therefore, the formation of M_F was the mainly hardening mechanism for the SZs, and grain refinement was the extra hardening mechanism for the FG-HAZ.

4.3. Material softening during welding

Fig. 3 and Table 2 showed that both of the joints exhibited conspicuous hardness valleys with the reduced value of ~80 Hv compared to the PM. Thereinto, the hardness of SC-HAZ decreased, while the IC-HAZ bridged the hardness variation of the SC-HAZ and the FG-HAZ. It should be noted that the minimum hardness point

was located at the boundary of the IC-HAZ and the SC-HAZ, which was the same as the FSW joint of DP 1180 steel [40].

4.3.1. IC-HAZ

In the IC-HAZ, there was no evident difference in the phase morphology, but the gradual increase of the ferrite volume fraction along with the regular diminution of temperature. Based on the temperature distributions in Fig. 8, the IC-HAZ was in A_{c3}-A_{c1} two-phase region, indicating that the ferrite to austenite transformation proceeded during the heating process. The results in Table 3 disclosed that the cooling rate of the IC-HAZ was higher than the minimum cooling rate for fully martensitic transformation. Thus all the descended austenite transformed into M_F in subsequent cooling, resulting in the formation of the DP structures. In the carbon distribution map shown in Fig. 12(b, e), these M_F was rich in carbon element after austenite/martensite transformation, signifying a solution hardening effect in this region. However, the volume fraction of M_F decreased and ferrite fraction increased with the temperature declining according to the lever rule in the binary alloy [41], as drawn in Fig. 7. Thus, it was well-understood that the gradually increased proportion of the soft ferrite led to the hardness reduction in the IC-HAZ.

4.3.2. SC-HAZ

In the SC-HAZ, the material softening was induced by several complicated factors. In the first place, lots of investigations have shown that martensite decomposition during the tempering process is the main reason for the softening of steel joints [42,43]. Differently, the carbide particles in this work were mainly precipitated along the PAGBs but hard to found inside the M_I, as verified by the carbon concentration in Fig. 12(e, f). Therefore, it is reasonable to infer that the tempering decomposition of the M_F played a vital role in the softening effect, while the M_I take the second place. This was relevant to the less stable microstructure of the M_F. The M_F possessed a higher density of dislocation and substructures, while the reversion process had proceeded in M_I via the partitioning treatment. Additionally, the M_F had a higher content of carbon element since the M_F was transformed from the carbon enriched austenite after partitioning treatment, as revealed in Fig. 12(a, d).

In the second place, the apparent decrease of the austenite fraction indicated that the evolution of austenite also got involved in the material softening (compare Fig. 4(b) with Fig. 6(e)). Recently, some studies [31,33] proposed that the retained austenite was harder than ferrite and/or bainite in steels due to higher element concentration (carbon or manganese). Besides, the austenite participated in partial hardness improvement via strain-induced martensite transformation. Hence the dissolution of retained austenite should additionally contribute to the material softening in the SC-HAZ.

In the third place, the decomposition of the M_F and austenite induced the formation of ferrite, which increased the volume fraction of the ferrite in the SC-HAZ compared to the PM (Fig. 7). The peak of ferrite fraction was corresponding with the lowest microhardness point in the microhardness distributions (Fig. 3). This indicated that the proportion enhancement of the ferrite was another crucial mechanism for the material softening in the SC-HAZ.

4.4. Strain hardening during tensile deformation

4.4.1. Microstructure strengthening

For the IC-HAZ, it has been well accepted that the DP structure owns high strain hardening ability. Calcagnotto et al. [30,44] proposed that the volume expansion during austenite-to-martensite transformation produced dislocation heterogeneities and residual
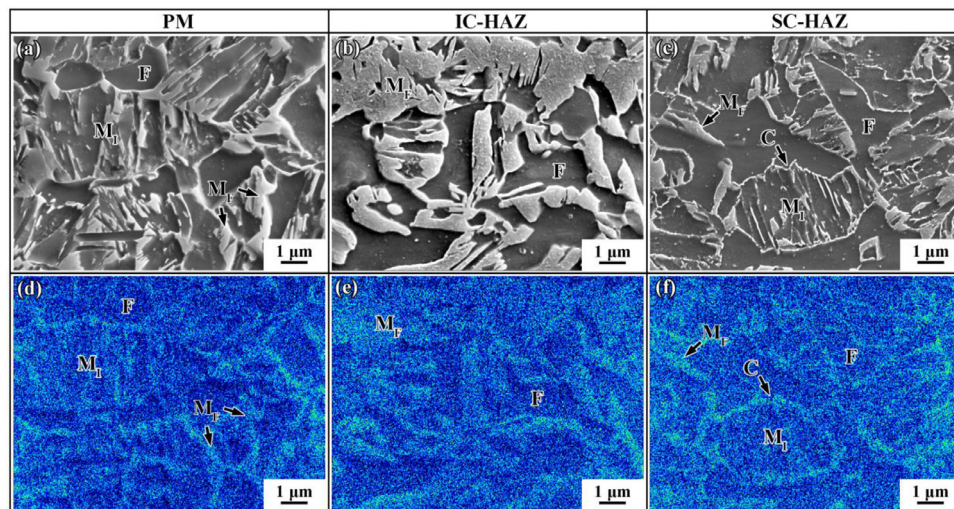
Fig. 12. EPMA analysis showing the element evolvement of the 450 rpm joint: (a–c) secondary electron images, (d–f) carbon element distribution maps.
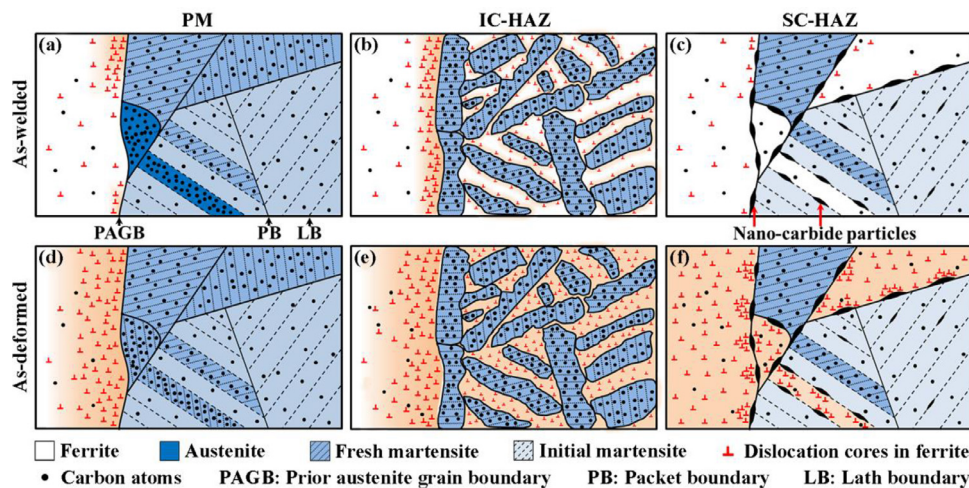

Fig. 13. Schematic sketch drawings of the microstructural evolutions during welding and post-weld tensile deformation.

stresses in ferrite. As shown in Fig. 13(b, e), the dislocation-dislocation interaction, dislocation pile-ups at ferrite/martensite interfaces, and the corresponding long-range elastic back stress will contribute to the rapid strain hardening and high UTS of the IC-HAZ, which has been summarized in a review by Zhao and Jiang [8].

In the SC-HAZ, complex microstructural evolution occurred during welding, including carbon clustering, dislocation restoration, decompositions of martensite and retained austenite. In this tempered zone, the dislocation heterogeneities and residual stress in the ferrite were reduced due to the reversion transformation (Fig. 13(a, c)). So the strength improvement via the DP structure was trivial. However, it was conceivable that the newly formed ultrafine ferrite and nano-carbide particles during the tempering transformation of M_I and austenite played crucial roles in facilitating the strengthening of the joints [31].

For one thing, the rapid multiplication and accumulation of dislocations in the ferrite at the early deformation stage could make significant contributions to its subsequent strain hardening (Fig. 13(f)). This inference could be attested by the microstructural observation after tensile deformation, while apparent dislocation accumulation was detected in the ultrafine ferrite (Fig. 14(a)). For another thing, the pinning and trapping effect on dislocations by the nano-carbide particles contributed to significant strain harden-

ing with the further deformation. As revealed in Fig. 14(b), numerous dislocation clusters were found adjacent to the carbide particles, which signified the interactions between dislocations and the carbide particles. Moreover, the M_I was expected to provide extra strain hardening in the SC-HAZ, as obvious enhancement of the hardening exponent n from 0.04 to 0.07 was found in the nanoindentation results (Fig. 10(b)).

4.4.2. Macrostructure strengthening

Special macrostructural configuration can provide extra strengthening for the welded joint. Some numerical results [32,45] indicated that in the laser butt welded DP 980 steel sheets, the stress in the softened zone changed from a uniaxial (σ_1) to a biaxial stress state (σ_1, σ_2), but the hardened zone and the PM remained in a uniaxial stress state (Fig. 15). Compared to the PM, the extra stress (σ_2) in the softened zone was a kind of constraint stress produced by the transverse strain component (along welding direction). The existence of the constraint stress could offset a portion of external stress, which was beneficial to improve the strength of the HAZ (here referred to the IC-HAZ and SC-HAZ) to the PM level and incline the plastic instability toward the PM region (Fig. 9(a, c)). However, overlarge HAZ could reduce the constraint stress, which led to a weak macrostructure
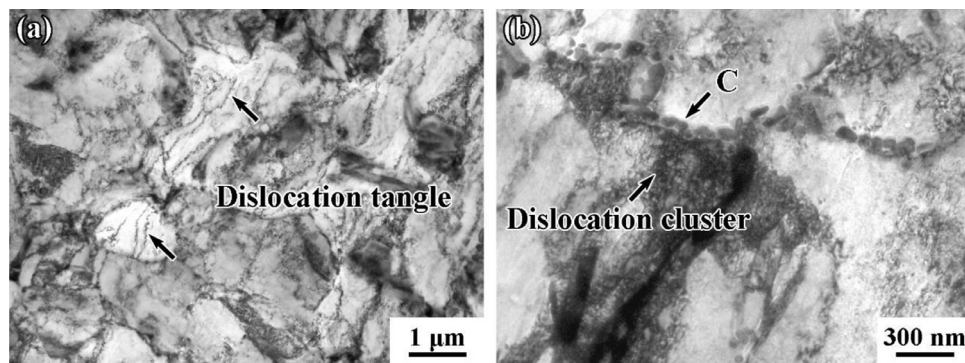
Fig. 14. TEM microstructures of the SC-HAZ after tensile deformation under 450 rpm parameter: (a) dislocation accumulation in the ferrites, (b) reciprocal action between dislocations and the carbide particles.
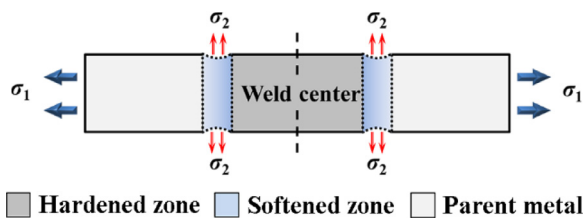

Fig. 15. Top surface schematic diagram showing the stress state of the joint's softened zone during tensile process.

strengthening effect and enabled premature strain localization and failure in the HAZ (Fig. 9(b, d)).

5. Conclusions

High-quality FSW joints were successfully fabricated in the Q&P 1180 steel under different rotation rates. The microstructures evolution and mechanical properties were carefully studied via multiple characterization routes. The main results are summarized as follows:

1. The defect-free joints with similar tensile strength to that of the PM were produced at rotation rates of both 450 rpm and 600 rpm, although considerable material softening occurred in the HAZ with microhardness drop of near 80 Hv. There was no evident variation in the minimum hardness value of the joints when increasing the rotation rate.
2. The FSW thermal cycle dominated the microstructural features across the joints. Single-phase M_F was formed in the SZs because the peak temperatures were over A_{c3} and the cooling rates were far above the minimum cooling rate for fully martensitic transformation. Based on the high cooling rates, DP structure comprised ferrite and M_F was generated in the IC-HAZ, and complex microstructural evolutions occurred in the SC-HAZ, including the decomposition of the metastable phases and the precipitation of the nano-carbide particles.
3. A HSZ-IPTL model was proposed to analyze the strength and the minimum hardness of the joints under different parameters. The formation of the M_F was the mainly hardening mechanism for the SZs. The gradually increased proportion of the ferrite led to the hardness reduction in the IC-HAZ, while the decomposition of the martensite and retained austenite promoted the softening of the SC-HAZ with the consequent fraction growth of the ferrite.
4. The mechanisms that contributed to the high UTS of the softened joints were complex. The DP structure, nano-carbide particles, tempered M_I, and newly formed ultrafine ferrite could be associated with improving the strain hardening ability of the

HAZ. The biaxial stress intensification was proposed to provide additional strength enhancement of the HAZ as well as determining the fracture location of the joints.

Supplementary materials

Supplementary material associated with this article can be found, in the online version, at doi:10.1016/j.jmst.2021.06.031.

References

[1] J. Speer, D.K. Matlock, B.C. De Cooman, J.G. Schroth, Acta Mater. 51 (2003) 2611–2622.
[2] A.J. Clarke, J.G. Speer, M.K. Miller, R.E. Hackenberg, D.V. Edmonds, D.K. Matlock, F.C. Rizzo, K.D. Clarke, E. De Moor, Acta Mater. 56 (2008) 16–22.
[3] J.G. Speer, F.C. Rizzo Assunção, D.K. Matlock, D.V. Edmonds, Mater. Res. 8 (2005) 417–423.
[4] X.D. Tan, Y.B. Xu, X.L. Yang, D. Wu, Mater. Sci. Eng. A 589 (2014) 101–111.
[5] I. de Diego-Calderon, I. Sabirov, J.M. Molina-Aldareguia, C. Fojer, R. Thiessen, R.H. Petrov, Mater. Sci. Eng. A 657 (2016) 136–146.
[6] M. Takahashi, ISIJ Int. 55 (2015) 79–88.
[7] J.H. Schmitt, T. Iung, C. R. Phys. 19 (2018) 641–656.
[8] J.W. Zhao, Z.Y. Jiang, Prog. Mater. Sci. 94 (2018) 174–242.
[9] G.K. Ahiale, Y.J. Oh, Mater. Sci. Eng. A 597 (2014) 342–348.
[10] C. Luo, Y. Cao, Y. Zhao, L. Zhao, J. Shan, Weld. J. 97 (2018) 214–228.
[11] W. Guo, Z.D. Wan, P. Peng, Q. Jia, G.S. Zou, Y. Peng, J. Mater. Process. Technol. 256 (2018) 229–238.
[12] W.D. Li, L.X. Ma, P. Peng, Q. Jia, Z.D. Wan, Y. Zhu, W. Guo, Mater. Sci. Eng. A 717 (2018) 124–133.
[13] R.S. Mishra, Z.Y. Ma, Mater. Sci. Eng. R 50 (2005) 1–78.
[14] Z.Y. Ma, A.H. Feng, D.L. Chen, J. Shen, Crit. Rev. Solid State Mater. Sci. 43 (2018) 269–333.
[15] P. Xue, Z.Y. Ma, Y. Komizo, H. Fujii, Mater. Lett. 162 (2016) 161–164.
[16] H. Zhang, P. Xue, D. Wang, L.H. Wu, D.R. Ni, B.L. Xiao, Z.Y. Ma, Mater. Lett. 242 (2019) 91–94.
[17] H. Zhang, P. Xue, D. Wang, L.H. Wu, D.R. Ni, B.L. Xiao, Z.Y. Ma, J. Mater. Sci. Technol. 35 (2019) 1278–1283.
[18] H. Zhang, D. Wang, P. Xue, L.H. Wu, D.R. Ni, B.L. Xiao, Z.Y. Ma, J. Mater. Sci. Technol. 34 (2018) 2183–2188.
[19] M. Matsushita, Y. Kitani, R. Ikeda, M. Ono, H. Fujii, Y.D. Chung, Sci. Technol. Weld. Join. 16 (2011) 181–187.
[20] H.T. Lin, H.T. Jiang, Y.S. Wang, S.W. Tian, Mater. Res. Express 6 (2019) 126584.
[21] H. Maruyama, J. Jpn. Soc. Heat Treat 17 (1977) 198–204.
[22] X.X. Zhang, D. Wang, B.L. Xiao, H. Andrae, W.M. Gan, M. Hofmann, Z.Y. Ma, Mater. Des. 115 (2017) 364–378.
[23] L.H. Wu, X.B. Hu, X.X. Zhang, Y.Z. Li, Z.Y. Ma, X.L. Ma, B.L. Xiao, Acta Mater. 166 (2019) 371–385.
[24] Y.L. Cai, S.L. Yang, Y.H. Wang, S.H. Fu, Q.C. Zhang, Mater. Sci. Eng. A 664 (2016) 155–164.

[25] Y. Gao, S.H. Fu, T. Cheng, X. Huo, Q.C. Zhang, in: Proceedings of the International Conference on Optics in Precision Engineering and Nanotechnology (icOPEN2013), SPIE, Singapore, 2013.

[26] C.Y. Wang, J. Shi, W.Q. Cao, H. Dong, Mater. Sci. Eng. A 527 (2010) 3442–3449.

[27] Q. Jia, W. Guo, Z.D. Wan, Y. Peng, G.S. Zou, Z.L. Tian, Y.N. Zhou, J. Mater. Process. Technol. 259 (2018) 58–67.

[28] D.K. Matlock, V.E. Bräutigam, J.G. Speer, Mater. Sci. Forum 426-423 (2003) 1089–1094.

[29] J. Trzaska, L.A. Dobrzański, J. Mater. Process. Technol. 192-193 (2007) 504–510.

[30] M. Calcagnotto, D. Ponge, D. Raabe, Mater. Sci. Eng. A 527 (2010) 7832–7840.

[31] Z.W. Wang, H. Zhang, X.H. An, L.H. Wu, P. Xue, Q.C. Zhang, D.R. Ni, B.L. Xiao, Z.Y. Ma, Mater. Sci. Eng. A 793 (2020) 139979.

[32] Q. Jia, W. Guo, W.D. Li, P. Peng, Y. Zhu, G.S. Zou, Y. Peng, Z.L. Tian, Mater. Sci. Eng. A 680 (2017) 378–387.

[33] S. Mironov, Y.S. Sato, S. Yoneyama, H. Kokawa, H.T. Fujii, S. Hirano, Mater. Sci. Eng. A 717 (2018) 26–33.

[34] G. Cheng, K.S. Choi, X. Hu, X. Sun, Mater. Sci. Eng. A 652 (2016) 384–395.

[35] M. Dao, N. Chollacoop, K.J. Van Vliet, T.A. Venkatesh, S. Suresh, Acta Mater. 49 (2001) 3899–3918.

[36] R. Rodriguez, I. Gutierrez, Mater. Sci. Eng. A 361 (2003) 377–384.

[37] J.L. Bucaille, A. Rossoll, B. Moser, S. Stauss, J. Michler, Mater. Sci. Eng. A 369 (2004) 82–92.

[38] F.C. Liu, Z.Y. Ma, Metall. Mater. Trans. A 39A (2008) 2378–2388.

[39] M. Ghosh, K. Kumar, R.S. Mishra, Mater. Sci. Eng. A 528 (2011) 8111–8119.

[40] Z.W. Wang, G.M. Xie, D. Wang, H. Zhang, D.R. Ni, P. Xue, B.L. Xiao, Z.Y. Ma, Acta Metall. Sin. (Engl. Lett.) 33 (2020) 58–66.

[41] W.F. Smith, J. Hashemi, Foundations of Materials Science and Engineering, 4th ed., Mcgraw-Hill International, New York, 2006.

[42] J.F. Wang, L.J. Yang, M.S. Sun, T. Liu, H. Li, Mater. Des. 97 (2016) 118–125.

[43] V.H. Baltazar Hernandez, S.K. Panda, M.L. Kuntz, Y. Zhou, Mater. Lett. 64 (2010) 207–210.

[44] M. Calcagnotto, D. Ponge, E. Demir, D. Raabe, Mater. Sci. Eng. A 527 (2010) 2738–2746.

[45] S.K. Panda, N. Sreenivasan, M.L. Kuntz, Y. Zhou, J. Eng. Mater. Technol. 130 (2008) 041003–041011.